

## Article

# Study of Dynamic Inductance Gradient of Augmented Electromagnetic Rail Launcher Considering High-Speed Motion of Armature

Rongge Yan <sup>1,2,\*</sup>, Kang An <sup>1,2</sup>, Qingxin Yang <sup>1,2</sup> and Jinbo Jiang <sup>1,2</sup>

<sup>1</sup> State Key Laboratory of Reliability and Intelligence of Electrical Equipment, Hebei University of Technology, Tianjin 300130, China; 202121401110@stu.hebut.edu.cn (K.A.); qxyang@tjut.edu.cn (Q.Y.); 202121401046@stu.hebut.edu.cn (J.J.)

<sup>2</sup> Key Laboratory of Electromagnetic Field and Electrical Apparatus Reliability of Hebei Province, Hebei University of Technology, Tianjin 300130, China

\* Correspondence: yanrg@hebut.edu.cn; Tel.: +86-136-4211-6378

**Abstract:** The rail inductance gradient is an important parameter of the electromagnetic launcher. The calculation of its value is important for the design of the launcher structure and for predicting the motion behavior of the armature. The current research on the inductance gradient analysis method of the electromagnetic rail launcher mostly does not take into account the effects of launcher size and current diffusion. This method cannot describe its dynamic characteristics, and it results in a large error compared with the actual launch. Therefore, the paper first establishes an electromagnetic rail launcher armature motion model to obtain the rail velocity skin depth under a U-shaped armature. Second, an analytical method for calculating the inductance gradient based on the dynamic skin depth of the rail is obtained, which takes into account the launcher size and velocity skin effect. Finally, the experimental results verify the correctness and accuracy of the method to achieve an accurate prediction of armature speed.

**Keywords:** augmented electromagnetic rail launcher; dynamic inductance gradient; velocity skin depth; analytical method



**Citation:** Yan, R.; An, K.; Yang, Q.; Jiang, J. Study of Dynamic Inductance Gradient of Augmented Electromagnetic Rail Launcher Considering High-Speed Motion of Armature. *Appl. Sci.* **2023**, *13*, 9028. <https://doi.org/10.3390/app13159028>

Academic Editor: Salvador G. Garcia

Received: 29 June 2023

Revised: 2 August 2023

Accepted: 3 August 2023

Published: 7 August 2023



**Copyright:** © 2023 by the authors. Licensee MDPI, Basel, Switzerland. This article is an open access article distributed under the terms and conditions of the Creative Commons Attribution (CC BY) license (<https://creativecommons.org/licenses/by/4.0/>).

## 1. Introduction

The electromagnetic rail launcher uses two or more pairs of rails to form the body of the rail launcher, where the main rail carries the armature movement and the other pair or pairs of secondary rails act as an enhancement to the magnetic field in the gun chamber. The inductance gradient, namely the inductance per unit length, is one of the most important parameters in determining the performance of the electromagnetic launcher system and is closely related to the armature speed as well as the energy conversion efficiency of the system, which is reflected in the literature [1,2]. Therefore, it is important to calculate the dynamic inductance gradient parameters of the electromagnetic rail launcher considering the high-speed motion of the U-shaped armature for predicting the armature velocity.

The literature [3] used the finite element method to obtain the inductance gradient of the enhanced four-rail electromagnetic launcher. The literature [4] obtained an inductance gradient by analyzing the average speed of the armature. The literature [5] studied the effect of rail radius on inductance gradient. The literature [6] researched the effect of rail size on the inductance gradient. However, the above methods were all based on finite element method research and could not directly obtain the inductance gradient.

The literature [7] mentioned that the high-speed motion of the armature caused the velocity skin effect and affected the magnetic field diffusion between the rails. The literature [8] calculated the inductance gradient, taking into account the dynamic skin depth, but it did not consider the speed of the armature. The literature [9] also took into

account the dynamic skin depth, but it did not consider the height of the armature. The literature [10] presented an analytical method for calculating the inductance gradient of electromagnetic rail launchers with complex structures.

The above studies of rail inductance gradients were all about conventional rail launchers, not electromagnetic rail launchers, and the obtained inductance gradient did not take into account the effects of launcher geometry and rail dynamic skin depth. This paper starts by establishing a mathematical model of the electromagnetic launcher considering the high-speed motion of the armature and deriving the equivalent rail dynamic skin depth under the U-shaped armature. The analytical calculation of the inductance gradient considering the launcher size and velocity skin effect is obtained by applying the Biot–Savard law. Finally, the theoretical, calculated values are compared with the experimental data to achieve an accurate prediction of the armature speed.

### 2. Modeling Dynamic Electromagnetic Emissions

The two-dimensional model of the electromagnetic rail launcher is shown in Figure 1. The pulse current  $I$  flows from the outer rails to the inner rail on one side. When the current passes through the armature, it flows back from the other inner rail. The pulse current generates the flux density  $B$ , which acts with the armature current to generate the electromagnetic thrust  $F_a$  to drive the armature movement with velocity  $v$ .

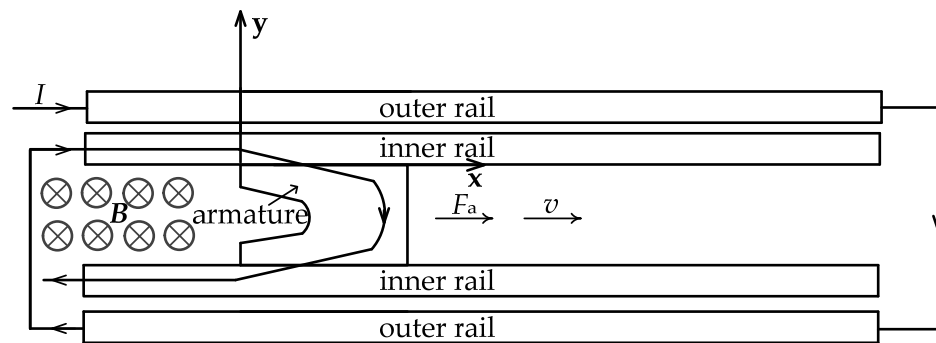


Figure 1. The electromagnetic rail launcher 2D model.

The current line distribution on the armature can be simplified, as shown in Figure 2.

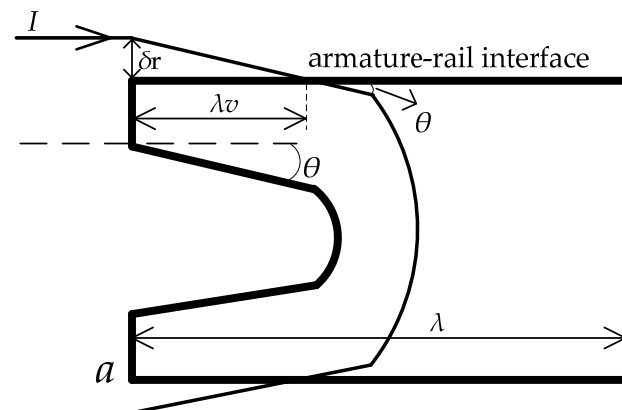


Figure 2. Armature current line distribution.

$\lambda$  is the length of the armature,  $\theta$  the angle of current flow into the armature,  $\delta_r$  the rail skin depth,  $\lambda_v$  the range of current inflow in the  $x$ -direction at the armature–rail interface, and  $a$  is the point on the armature tail, whose horizontal coordinate range is  $x_a \geq 0$ .

The magnetic diffusion equation for the inner rail is

$$\frac{1}{\mu_0\sigma_r} \left( \frac{\partial^2 \mathbf{B}_r}{\partial x^2} + \frac{\partial^2 \mathbf{B}_r}{\partial y^2} \right) = \frac{\partial \mathbf{B}_r}{\partial t} \tag{1}$$

where  $\mu_0$  is the vacuum magnetic permeability,  $\mathbf{B}_r$  is the flux density on the inner rail, and  $\sigma_r$  the electrical conductivity of the inner rail material.

Since  $\mathbf{B}_r$  varies in the inner rail more rapidly in the  $y$ -direction than in the  $x$ -direction, we can simplify Equation (1) by neglecting  $\partial^2 \mathbf{B}_r / \partial x^2$  relative to  $\partial^2 \mathbf{B}_r / \partial y^2$  obtain a simple diffusion-like equation.

$$\frac{1}{\mu_0\sigma_r} \frac{\partial^2 \mathbf{B}_r}{\partial y^2} = \frac{\partial \mathbf{B}_r}{\partial t} \tag{2}$$

A section of displacement  $\Delta x$  ( $0 \leq \Delta x \leq \lambda$ ) is taken on the inner rail at the armature–rail interface ( $x_a \leq x \leq x_a + \lambda$ ), as shown in Figure 3.

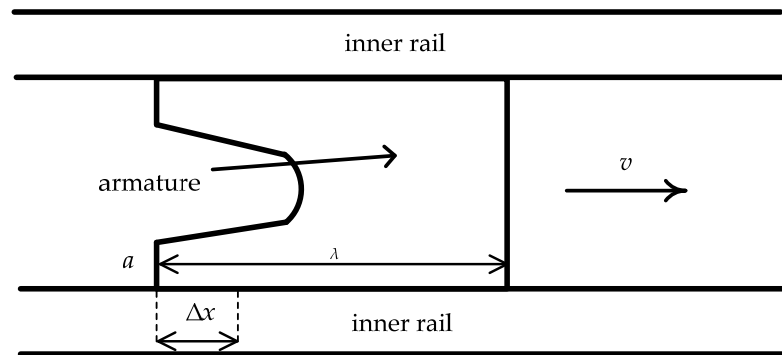


Figure 3. The armature–rail interface.

Since the speed of the armature is very fast, when the armature goes through the displacement  $\Delta x$ , the flux density on the inner rail can be treated as

$$\frac{1}{\mu_0\sigma_r} \frac{\partial^2 \mathbf{B}_r}{\partial y^2} = v \frac{\partial \mathbf{B}_r}{\partial (\Delta x)} \tag{3}$$

According to the boundary conditions of the armature in the conventional rail launcher in the literature [11], the boundary conditions of the armature of the electromagnetic rail launcher in this paper are set as follows.

$$\begin{cases} \mathbf{B}_a(x_a, y) = \mathbf{B}_0 + \mathbf{B}' \\ \left. \frac{\partial \mathbf{B}_a}{\partial y} \right|_{y=-\frac{s}{2}} = 0 \\ \mathbf{B}_a(x_a + \lambda, y) = \mathbf{B}' \end{cases} \tag{4}$$

where  $\mathbf{B}_a$  is the flux density on the armature,  $\mathbf{B}_0$  is the flux density generated by the armature tail current density, and  $\mathbf{B}'$  is the flux density generated by the outer rail on the armature. Since the outer rail current loop does not vary with the armature displacement, which can be regarded as  $\mathbf{B}'$  independent of the armature position,  $s$  the distance between the two inner rails.

Set the armature tail current density as  $\mathbf{J}_0$ ; then, the current density decay of the armature along the  $y$ -direction at a distance  $\Delta x$  from the tail is

$$J_{ay} \Big|_{x=\Delta x} = -J_0 e^{-\Delta x / \lambda_v} \tag{5}$$

According to Ampere’s loop theorem, the flux density  $B_{a1}(\Delta x)$  on the armature generated by  $J_{ay}$  can be obtained as

$$B_{a1}(\Delta x) = -\mu_0 \int J_{ay} d(\Delta x) \tag{6}$$

Combining Equation (6), we can approximate the flux density  $B_i(\Delta x)$  at the armature–rail interface as

$$B_i(\Delta x) = B_0 [e^{-\Delta x/\lambda_v} - \frac{\Delta x}{\lambda} e^{-\lambda/\lambda_v}] + B' \tag{7}$$

### 3. Deriving the Rail Skin Depth under the U-Shaped Armature

Because of the skin effect, the currents on both the rail and the armature tend to be surface-distributed. When the velocity skin effect is significant, there is  $\lambda_v \ll \lambda$ , which is reflected in the literature [12]. Then, the average current density along  $x$ - and  $y$ -directions ( $J_{rx}$  and  $J_{ry}$ , respectively) in the inner rail side is taken as  $\lambda_v$ . Combining the geometric relations in Figure 2 yields.

$$\tan \theta = -\overline{J_{ry}}/\overline{J_{rx}} = \int_0^{\Delta x} \frac{\partial B_r}{\partial x} \Big|_{y=0+d(\Delta x)} / \int_0^{\Delta x} \frac{\partial B_r}{\partial y} \Big|_{y=0+d(\Delta x)} \tag{8}$$

The solution to the type of equation given by Equation (3) is

$$B_r(\Delta x, y) = \int_0^{\Delta x} \frac{dB_i(\xi)}{d\xi} \operatorname{erfc} \left\{ \frac{y}{2[\mu_0 \delta_r v (\Delta x - \xi)]^{1/2}} \right\} d\xi \tag{9}$$

From the same geometric relationship in Figure 2, we obtain

$$\tan \theta = \frac{\lambda_v}{\sigma_r} \tag{10}$$

Combining Equations (8)–(10), we can obtain

$$\begin{cases} \delta_v = \frac{1}{1.21^2 \tan \theta} \cdot \frac{1}{\mu_0 \sigma_r v} \\ \tan \theta = 1.21 \sqrt{\frac{1}{\mu_0 \sigma_r v \lambda_v}} \end{cases} \tag{11}$$

Figure 4 shows the actual current waveform in the experimental setup obtained by the current acquisition system, which indicates that the armature discharge time is about 1.531 ms. The actual current waveform can be approximated as a sawtooth wave, and its frequency can be regarded as 1/2 of the sinusoidal waveform according to the literature [13].

The skin depth of the rail with the sinusoidal current can be obtained as

$$\delta_{\sin} = \sqrt{\frac{1}{\pi \mu_0 \sigma_r f}} \tag{12}$$

where  $f = \frac{1}{2 \times 1.531}$  kHz is the current frequency according to Figure 4.

The literature [14] proved that when the armature speed is low, the current skin effect dominates. When the armature speed exceeds the critical speed  $v_c$ , the velocity skin effect starts to be significant, so the equivalent skin depth can be obtained as

$$\begin{cases} \delta_r = \delta_{\sin}, & v \leq v_c \\ \delta_r = \sqrt{\frac{1}{\pi \mu_0 \sigma_r} \cdot \frac{s_v}{v}}, & v > v_c \end{cases} \tag{13}$$

where  $s_v = k\lambda$  is the effective length of the armature contact current and  $k$  is the scale factor.

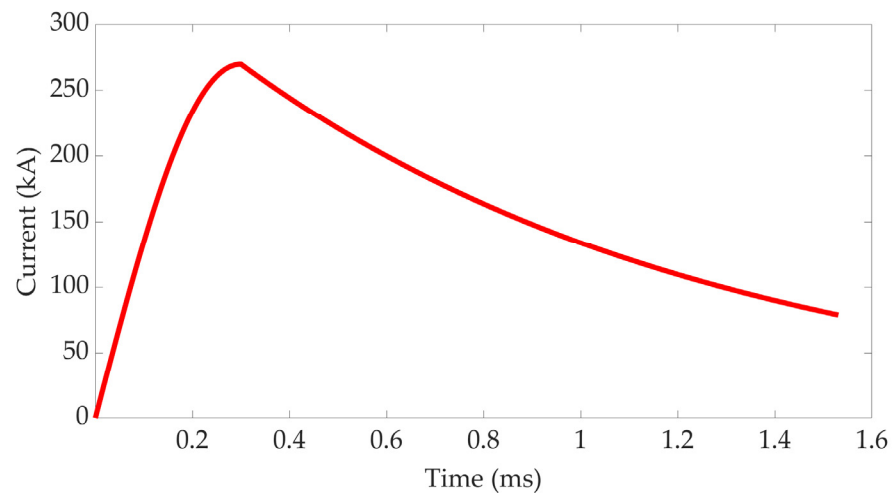


**Figure 4.** The pulse current waveform.

From Equations (11) and (13), we can obtain  $k = 2.42^2$ , and according to the literature [14],  $v_c = 150$  m/s.

Assuming that  $v \leq v_c$  and substituting  $\sigma_r = 5.998 \times 10^7$  S/m into Equation (13), the skin depth is about 3.6 mm, so the effect of skin depth should not be neglected for a rail width of 10 mm.

It can also be seen from Equation (13) that, during the launching process, the current skin effect plays a major role when the armature speed is less than the critical speed. After the armature speed exceeds the critical speed, the effect of the velocity skin effect is much larger than the current skin effect. As shown in Figure 5, obtaining the current density cloud map in the simulation software LSDYNA student version when the speed of the armature is 30 m/s, the current distribution in the rail is more uniform, and the skin depth is deeper. However, at a speed of 200 m/s of the armature, the current in the inner rail tends to be distributed on the surface, and the skin collection depth becomes shallow.

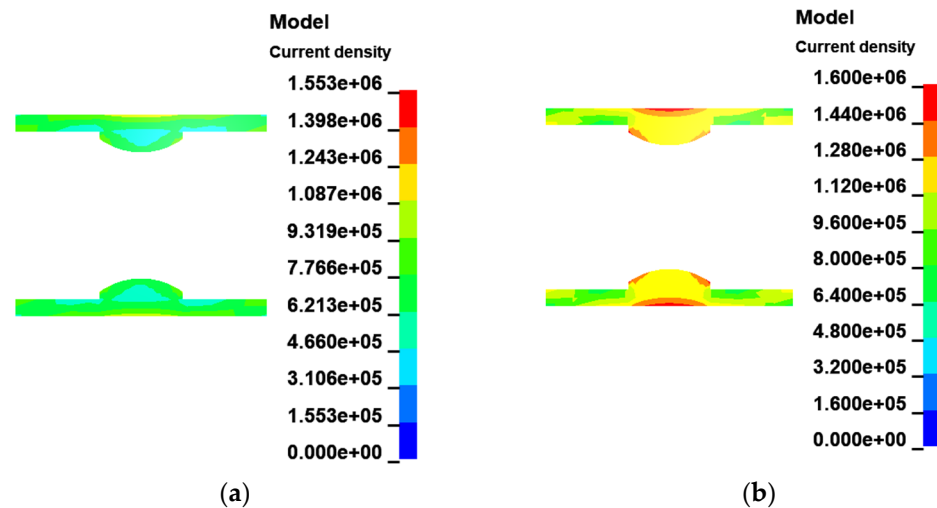


**Figure 5.** The cross-sectional current distribution of the rail: (a) The cross-sectional current distribution of the rail at an armature speed of 30 m/s; (b) the cross-sectional current distribution of the rail at an armature speed of 200 m/s.

#### 4. Calculating Dynamic Inductance Gradient

The equivalent inductance gradient of the augmented electromagnetic rail launcher is

$$L' = L'_c + 2M' \tag{14}$$

where  $L'$  is the equivalent inductance gradient,  $L'_c$  the inductance gradient of the inner rail, and  $M'$  the gradient of mutual inductance of the inner and outer rails.

The equation for the electromagnetic thrust of the armature is

$$F_a = F_c + F_M = \frac{(L'_c + 2M')I^2}{2} \tag{15}$$

where  $F_c$  is the electromagnetic thrust generated by the inner rail on the armature and  $F_M$  is the electromagnetic thrust generated by the outer rail on the armature.

From Equation (15), it is known that the electromagnetic thrust of the inner and outer rails for the armature can be obtained separately, and then, the inductance gradient of the inner rail and the mutual inductance gradient of the inner and outer rails can be obtained.

An alternative expression for the electromagnetic thrust of the armature is

$$F_a = B_{ay}Is \tag{16}$$

Assuming that the point  $p(x_p, y, z)$  is any point on the armature, Equation (16) can be approximated by combining the geometric relationship of the electromagnetic launcher:

$$F_a = \frac{I}{h_a} \int_0^s \int_{\frac{h-h_a}{2}}^{\frac{h+h_a}{2}} B_{ay} dy dz \tag{17}$$

where  $h$  is the height of the rail and  $h_a$  is the height of the armature.

The cross-sectional shape of the inner rail is similar to that of a T-rail, and the equivalent transformation of Figure 6 can be carried out to facilitate the calculation.

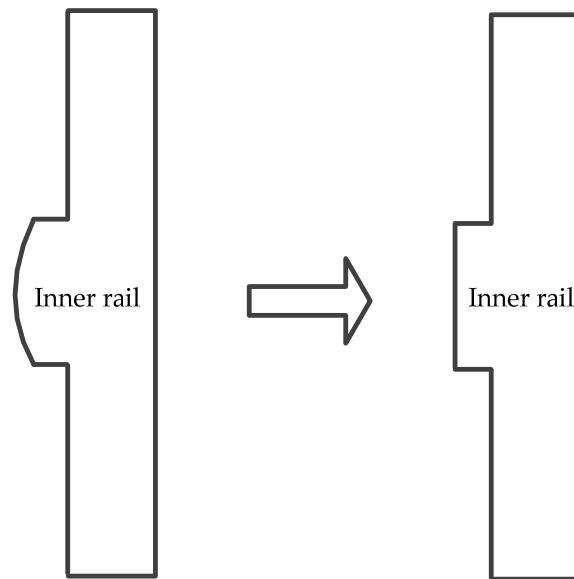


**Figure 6.** The equivalent transformation of inner rail section.

The current is concentrated on the rail surfaces in the actual working condition, so the equivalent diagram of the current distribution in the rail section is constructed as shown in Figure 7, assuming that the current is uniformly distributed in the shaded area, in which the width of each rectangle is the rail skin depth  $\delta_r$ .

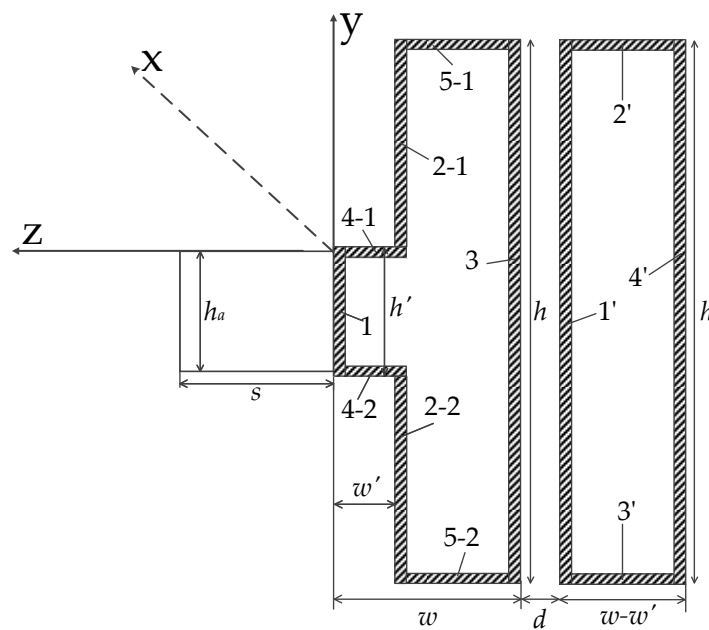


**Figure 7.** The equivalent armature–rail cross-section, where  $w$  is the thickness of the inner rail,  $h'$  the height of the trapezoidal part,  $w'$  the thickness of the trapezoidal part, and  $d$  is the distance between the inner rail and the outer rail.

4.1. The Inductance Gradient of the Inner Rail

An example of an inner railgun region 1 in Figure 6 is shown in Figure 8, where  $p$  and  $q$  are located on the armature and the inner rail, respectively.

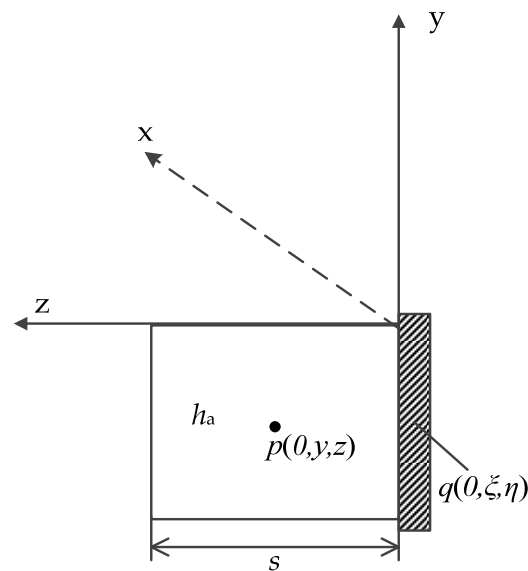


**Figure 8.** The cross-sectional view of the armature and area 1 of the inner rail.

The specific dimensions of the electromagnetic rail launcher are shown in Table 1.

**Table 1.** The specific dimensions of the electromagnetic rail launcher.

Physical Quantities	Size (mm)
s	12.88
w	10.5
w'	4.5
h	30
h'	10
h <sub>a</sub>	9.9
d	2

Combined with the specific dimensions of the rails in Table 1, the variation of the current region with the skin depth between 0 and 3.6 mm was obtained for the inner rail and outer rails, as shown in Figures 9 and 10.

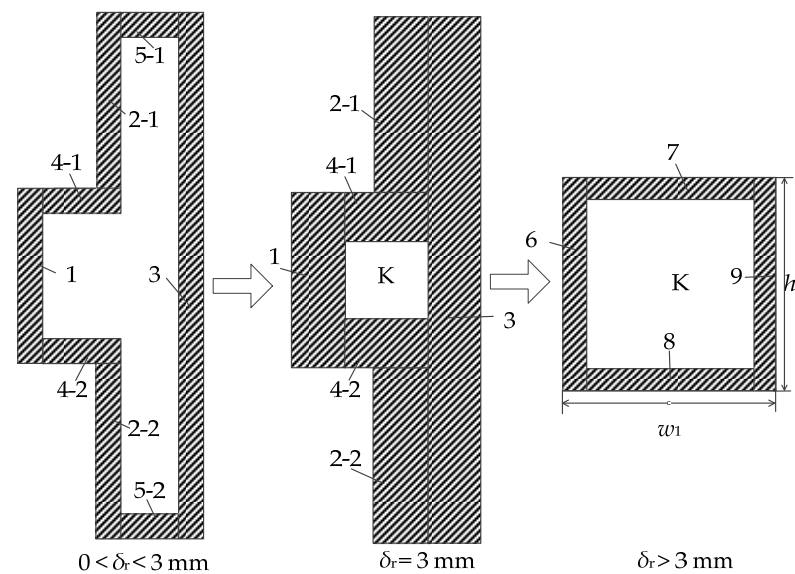


**Figure 9.** The current region of the inner rail varies with the skin depth.

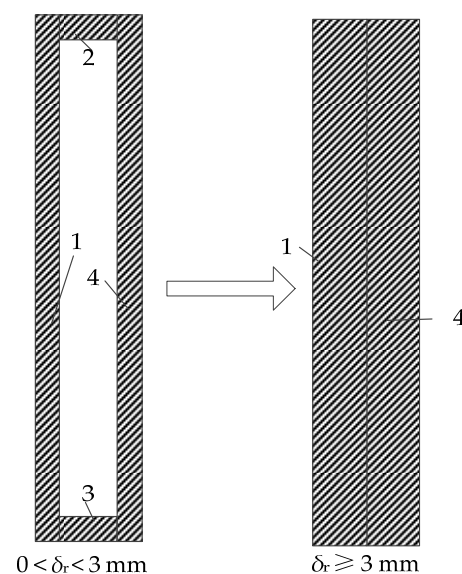


**Figure 10.** The current region of the outer rail varies with the skin depth.

As can be seen in Figure 9, because  $w - w' = 6\text{ mm}$ , the current region of rail 5 is occupied by rail 2 and rail 3 when the skin depth is greater than 3 mm. In addition, the

current regions of rail 2 and rail 3 are maximized. Therefore, the inductance gradient of rail 2, rail 3, and rail 5 no longer change in this stage. At the same time, a new rail 6 is generated, where  $h_6$  is the height of rail 6.

As can be seen in Figure 10, because  $w - w' = 6\text{mm}$ , the current region of rail 2 and rail 3 are occupied by rail 1' and rail 4' when the skin depth is greater than 3 mm, and the current regions of rail 1 and rail 4 are maximized. Therefore, the mutual gradient of rail 1' and rail 4' no longer change in this stage.

The magnetic induction in the  $y$ -direction produced by the right-hand rail on  $p$  is obtained from the Biot-Savard:

$$\begin{cases} B_{1y} = \frac{\mu_0}{4\pi} \frac{I}{I_S} \int_0^{\sigma_r} \int_{\frac{h-h'}{2}}^{\frac{h+h'}{2}} \frac{(\eta+z)k(l)}{(\eta+z)^2+(\xi-y)^2} d\xi d\eta \\ B_{2y} = \frac{\mu_0}{4\pi} \frac{I}{I_S} \left( \int_{w'}^{w'+\sigma_r} \int_{\frac{h-h'}{2}}^h \frac{(\eta+z)k(l)}{(\eta+z)^2+(\xi-y)^2} d\xi d\eta + \int_{w'}^{w'+\sigma_r} \int_0^{\frac{h-h'}{2}} \frac{(\eta+z)k(l)}{(\eta+z)^2+(\xi-y)^2} d\xi d\eta \right) \\ B_{3y} = \frac{\mu_0}{4\pi} \frac{I}{I_S} \int_{w-\sigma_r}^w \int_0^h \frac{(\eta+z)k(l)}{(\eta+z)^2+(\xi-y)^2} d\xi d\eta \\ B_{4y} = \frac{\mu_0}{4\pi} \frac{I}{I_S} \left( \int_{\sigma_r}^{w'} \int_{\frac{h-h'}{2}-\sigma_r}^{\frac{h+h'}{2}} \frac{(\eta+z)k(l)}{(\eta+z)^2+(\xi-y)^2} d\xi d\eta \right) + \int_{\sigma_r}^{w'} \int_{\frac{h-h'}{2}+\sigma_r}^{\frac{h+h'}{2}} \frac{(\eta+z)k(l)}{(\eta+z)^2+(\xi-y)^2} d\xi d\eta \\ B_{5y} = \frac{\mu_0}{4\pi} \frac{I}{I_S} \int_{w'+\sigma_r}^{w-\sigma_r} \int_{\sigma_r}^{h-\sigma_r} \frac{(\eta+z)k(l)}{(\eta+z)^2+(\xi-y)^2} d\xi d\eta \end{cases} \quad (18)$$

where  $k(l) = l / \sqrt{l^2 + (\eta + z)^2 + (\xi - y)^2}$  and  $l$  is the armature motion displacement. Since  $l$  is much larger than the other parameters,  $k(l)$  can be considered approximately 1.  $I_S = 2\sigma_r(h + w - 3\sigma_r)$  is the area of the current region of the skin depth  $<3$  mm. When the skin depth is  $\geq 3$  mm,  $I_S = (w - w_1)[h + w - (w - w_1)] + 2\sigma_r'(h + w - 2\sigma_r')$ .

When the skin depth  $\geq 3$  mm, the magnetic induction in the  $y$ -direction produced by the right-hand rail on the  $p$  is obtained from the Biot-Savard:

$$\begin{cases} B_{6y} = \frac{\mu_0}{4\pi} \frac{I}{I_S} \int_{w_1'}^{w_1'+\sigma_r'} \int_{\frac{h-h_1}{2}}^{\frac{h+h_1}{2}} \frac{(\eta+z)k(l)}{(\eta+z)^2+(\xi-y)^2} d\xi d\eta \\ B_{7y} = \frac{\mu_0}{4\pi} \frac{I}{I_S} \int_{w'}^{w'+\sigma_r'} \int_{\frac{h-h_1}{2}-\sigma_r'}^{\frac{h+h_1}{2}} \frac{(\eta+z)k(l)}{(\eta+z)^2+(\xi-y)^2} d\xi d\eta \\ B_{8y} = \frac{\mu_0}{4\pi} \frac{I}{I_S} \int_{w-\sigma_r}^w \int_{\frac{h-h_1}{2}+\sigma_r'}^{\frac{h+h_1}{2}} \frac{(\eta+z)k(l)}{(\eta+z)^2+(\xi-y)^2} d\xi d\eta \\ B_{9y} = \frac{\mu_0}{4\pi} \frac{I}{I_S} \int_{w_1'+w_1-\sigma_r'}^{w_1'+w_1} \int_{\frac{h-h_1}{2}}^{\frac{h+h_1}{2}} \frac{(\eta+z)k(l)}{(\eta+z)^2+(\xi-y)^2} d\xi d\eta \end{cases} \quad (19)$$

where  $\delta_r'$  is the skin depth of the region  $K$  and  $w_1' = (w+w')/2$  is the area of the current region.

According to Equations (15) and (17), as well as symmetry, the expression for the induced gradient for each inner rail ( $L'_{ci}$ ,  $i = 1,2,3,4,5,6$ ) is obtained as

$$L'_{ci} = \frac{4I}{h_a} \int_0^s \int_{\frac{h-h_a}{2}}^{\frac{h+h_a}{2}} B_{iy} dy dz \quad (20)$$

According to the size of the electromagnetic launcher in Table 1 and Equation (20), the variation law of  $L'_{ci}$  with the skin depth can be obtained, as shown in Figure 11.

According to each equivalent inner rail in Figure 9, it is known that the areas enclosed in rails 2–4 increase with increasing the skin depth, which increases the magnetic chain generated at the same current. Because  $h-h' = 0.001$  mm,  $L'_{c1}$  decreases with increasing the skin depth. However, the area enclosed by rail 5 decreases with increasing the skin depth, which is because the current region of rail 5 is affected by both rails 2 and 3. This results in a decrease in the area enclosed between the rail, causing a reduction in the magnetic chain generated at the same current. Considering the engineering reality, when the skin depth exceeds 3 mm, the value of  $L'_{c5}$  becomes 0. In addition, the values of  $L'_{c1}$ ,  $L'_{c2}$ ,  $L'_{c3}$ , and  $L'_{c4}$  increase rapidly with the increase of the skin depth because the  $I_S$  increases slowly

with the skin depth. Because the change in  $L'_{c6}$ ,  $L'_{c7}$ ,  $L'_{c8}$ , and  $L'_{c9}$  are very small, they can be seen as part of  $L'_{c1}$ ,  $L'_{c2}$ ,  $L'_{c4}$ ,  $L'_{c5}$  and not represented in Figure 11.

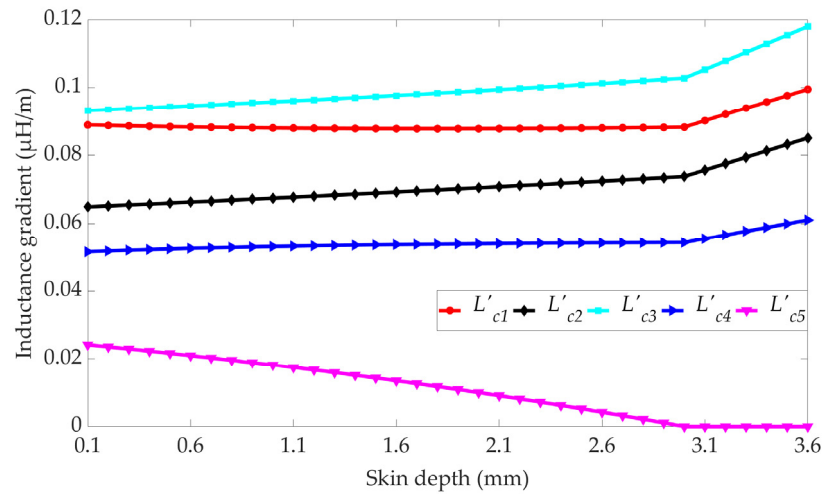


Figure 11. The variation law of  $L'_{ci}$  with the skin depth.

#### 4.2. The Gradient of Mutual Inductance of the Inner and Outer Rail

In this paper, the mutual inductance gradients of each equivalent rail in the outer rail and the inner rail are obtained sequentially by applying the method in Section 4.1 from an energy point of view. Unlike the inner rail, the current circuit of the outer rail does not change with the armature position; then, we can obtain the magnetic induction produced by each commuted outer rail at point p:

$$\begin{cases} B'_{1y} = \frac{\mu_0}{4\pi} \frac{I}{l'_s} \int_0^{\sigma_r} \int_{w+d}^{w+d+r} \int_0^h \frac{(\eta+z)[k(l)+k'(l)]}{(\eta+z)^2+(\xi-y)^2} d\xi d\eta dr \\ B'_{2y} = \frac{\mu_0}{4\pi} \frac{I}{l'_s} \int_0^{\sigma_r} \int_{w+d}^{w+d+w-w'-r} \int_0^{h-r} \frac{(\eta+z)[k(l)+k'(l)]}{(\eta+z)^2+(\xi-y)^2} d\xi d\eta dr \\ B'_{3y} = \frac{\mu_0}{4\pi} \frac{I}{l'_s} \int_0^{\sigma_r} \int_{w+d+r}^{w+d+w-w'-r} \int_r^{h-r} \frac{(\eta+z)[k(l)+k'(l)]}{(\eta+z)^2+(\xi-y)^2} d\xi d\eta dr \\ B'_{4y} = \frac{\mu_0}{4\pi} \frac{I}{l'_s} \int_0^{\sigma_r} \int_{w+d+w-w'-r}^{w+d+w-w'-r} \int_0^h \frac{(\eta+z)[k(l)+k'(l)]}{(\eta+z)^2+(\xi-y)^2} d\xi d\eta dr \end{cases} \quad (21)$$

where  $l'_s = 2\sigma_r(h+w-2\sigma_r)$ ,  $k'(l) = (L-l)/\sqrt{(L-l)^2+(\eta+z)^2+(\xi-y)^2}$  and L is the length of the rail. Since L is much larger than the other parameters,  $k'(l)$  can be considered approximately 1. When  $3\text{ mm} < \delta_r \leq 3.6\text{ mm}$ ,  $B'_{iy}$  ( $i = 1,2,3,4$ ) remains unchanged.

Similarly, we obtain the expression for the gradient of the mutual inductance of each equivalent rail in the outer rail relative to the inner rail ( $M'_{i'}$ ,  $i = 1,2,3,4$ ), which is

$$M'_{i'} = \frac{2I}{h_a} \int_0^s \int_{\frac{h-h_a}{2}}^{\frac{h+h_a}{2}} B_{ay} dy dz \quad (22)$$

The variation of  $M'_{i'}$  with skin depth is the same as that of  $L'_{ci}$  with skin depth, as shown in Figure 12.

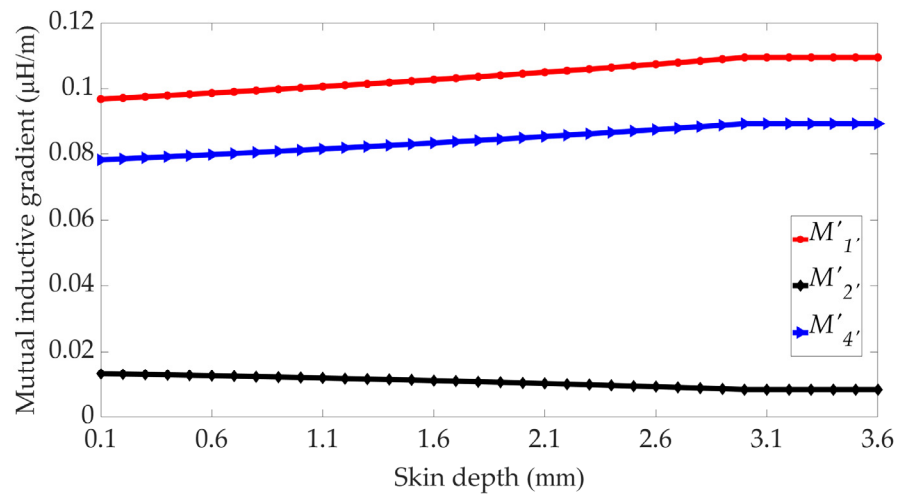


**Figure 12.** The variation law of  $M'_{1'}$  with the skin depth.

When the skin depth varies between 0.1 and 3 mm,  $M'_{c1'}$ ,  $M'_{c2'}$ , and  $M'_{c4'}$  increase with the increase of the skin depth. However, when the skin depth exceeds 3 mm,  $M'_{c1'}$ ,  $M'_{c2'}$ , and  $M'_{c4'}$  do not change anymore because  $w - w' = 6\text{mm}$ . During this period,  $M'_{c2'} = 0$ . According to each equivalent outer rail in Figure 6, it is known that rail 2' and rail 3' have the same pattern of change, owing to symmetry. Therefore, only three curves  $M'_{c1'}$ ,  $M'_{c2'}$ , and  $M'_{c4'}$  are shown in Figure 12.

#### 4.3. Equivalent Inductance Gradient

Since the inner and outer rails pass into the same directional current, the inner rail current is mainly concentrated on the inner surface, and the outer rail current is mainly concentrated on the outer surface.

Then, the current distribution in each region of Figure 7 can be expressed as

$$\left\{ \begin{array}{l} I_1 = c_1 \frac{h'l\sigma_r}{I_S l} I = \frac{c_1 h' I}{2(h+w-2\sigma_r)} \\ I_2 = c_1 \frac{(h-h')l\sigma_r}{I_S l} I = \frac{c_1 (h-h') I}{2(h+w-2\sigma_r)} \\ I_3 = c_2 \frac{hl\sigma_r}{I_S l} I = \frac{c_2 h I}{2(h+w-2\sigma_r)} \\ I_4 = c_1 \frac{w'l\sigma_r}{I_S l} I = \frac{c_1 w' I}{2(h+w-2\sigma_r)} \\ I_5 = c_3 \frac{(w-w'-2\sigma_r)l\sigma_r}{I_S l} I = \frac{c_3 (w-w'-2\sigma_r) I}{2(h+w-2\sigma_r)} \\ I'_1 = c'_1 \frac{hl\sigma_r}{I_S l} I = c'_1 \frac{c_1 h I}{2(h+w-2\sigma_r)} \\ I'_2 = c'_2 \frac{(2w-w'-d-2\sigma_r)l\sigma_r}{I_S l} I = \frac{c'_2 (2w-w'-d-2\sigma_r) I}{2(h+w-2\sigma_r)} \\ I'_4 = c'_4 \frac{hl\sigma_r}{I_S l} I = c'_4 \frac{c_1 h I}{2(h+w-2\sigma_r)} \\ I'_2 = I'_3 \end{array} \right. \quad (23)$$

where  $c_1, c_2, c_3, c'_1, c'_2$ , and  $c'_3$  are characterized as current distribution coefficients that satisfy the following conditions:

$$\left\{ \begin{array}{l} I = \sum_{i=1}^5 I_i \\ I = \sum_{i=1}^4 I'_i \end{array} \right. \quad (24)$$

Then,  $L'_c$  and  $M'$  can be expressed as follows:

$$\left\{ \begin{array}{l} L'_c = c_1(L'_{c1} + L'_{c2} + L'_{c4}) + c_2 L'_{c3} + c_3 L'_{c5} \\ M' = c'_1 M'_{1'} + c'_2 M'_{2'} + c'_3 (M'_{3'} + M'_{4'}) \end{array} \right. \quad (25)$$

In the literature [15], the current distribution coefficients on the rail are  $c_1 = 1.5$  and  $c_2 = 0.5$ . According to the current distribution in the simulation results, this paper takes  $c'_1 = 0.4$  and  $c'_2 = 1.8$ . Combining this with Equation (24), we obtain:

$$\begin{cases} c_3 = \frac{(w-w'-2\sigma_r)}{((w-w'-2\sigma_r)+(c_1-1)w')} \\ c'_3 = \frac{(2w-w'-d-2\sigma_r)}{((2w-w'-d-2\sigma_r)+(c'_1+c'_2-2)h)} \end{cases} \quad (26)$$

Substituting these four parameters into Equations (13) and (25), we can obtain the variation law of the inner rail inductance gradient, outer rail mutual inductance, and rail equivalent inductance gradient with the skin depth, as shown in Figure 13.

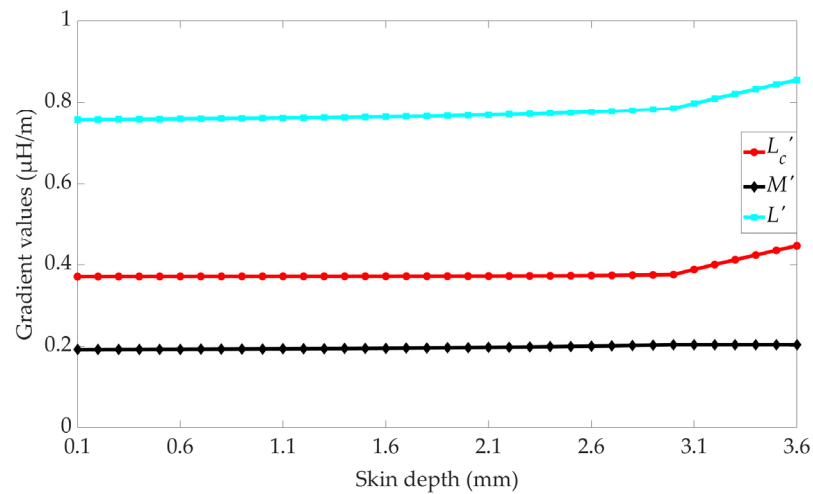


Figure 13. The variation law of  $L_c'$ ,  $M'$ , and  $L'$  with the skin depth.

In Figure 13, we observe that the inner rail inductance gradient, outer rail mutual inductance, and rail equivalent inductance gradient all increase with the increase of skin depth. When the skin depth is less than 3 mm, the inner rail inductance gradient, the outer rail mutual inductance, and the rail equivalent inductance gradient increase with the increase of skin depth. However, when the skin depth exceeds 3 mm, the outer rail mutual inductance remains constant with a value of about 0.2042 μH/m. In this stage, the inner rail inductance gradient and the rail equivalent both increase suddenly with the increase of skin depth because  $I_s$  increases slowly with the skin depth.

### 5. Experimental Results Analysis

The equation of motion of the armature is given by

$$\begin{cases} v = \frac{F_a - \mu_v(F_0 + F_N + F_P) - f_p}{m} \cdot t \\ l = \int_0^t v dt \end{cases} \quad (27)$$

where  $\mu_v$  is the Poisson's ratio,  $F_0$  is the armature and rail initial contact pressure,  $F_N = \frac{\mu S_c}{2(1-\mu)S} F_a$  is the electromagnetic pressure of the armature,  $F_P = \frac{\mu S_c}{2(1-\mu)S} f_p$  is the air pressure,  $f_p = \frac{\gamma+1}{2} \rho_0 (Sv^2 + Sla + \frac{c_f \lambda v^2 l}{2})$  is the air resistance,  $m$  is the mass of the armature,  $S_c$  is the armature and the rail contact area,  $S$  is the cross-sectional area of the armature,  $\lambda$  is the specific heat ratio,  $c_f$  is the coefficient of friction of air-adhesive tape, and  $\rho_0$  is the air density.

Passing the pulse current in Figure 4 and combining Equations (13) and (25), the relationship between the inductance gradient and the armature electromagnetic thrust with time, as well as the armature velocity and the armature displacement with time, can be obtained, as shown in the Figures 14 and 15.

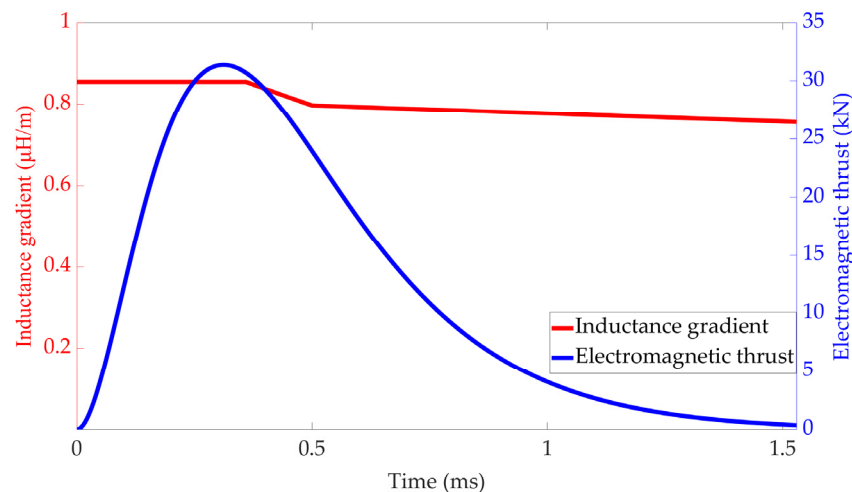


**Figure 14.** Theoretical inductance gradient and electromagnetic thrust of the armature curves.

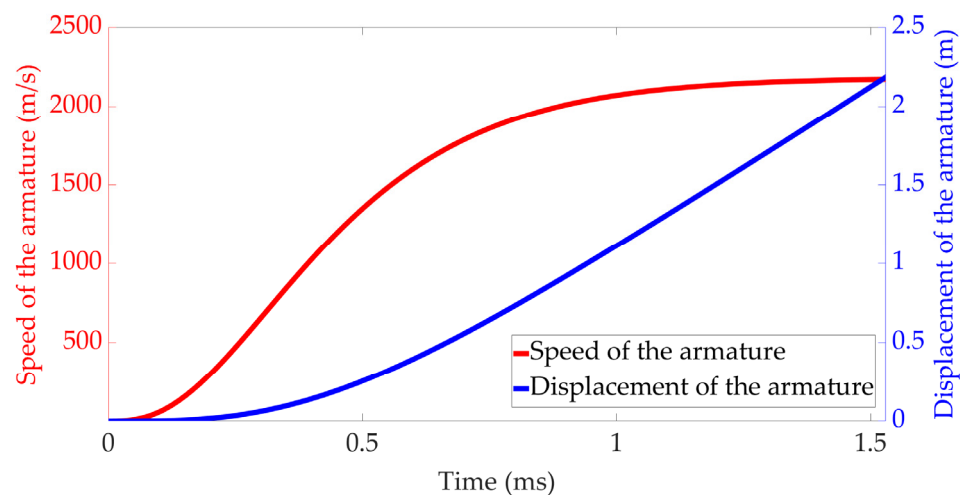


**Figure 15.** Theoretical speed of the armature and displacement of the armature curves.

In Figure 14, since the dynamic skin depth is considered, the obtained inductance gradient is time-varying, which is completely different from the results in the literature [7–9]. In the early stage of launch, the skin depth is deeper, so the calculated inductance gradient is about  $0.8549 \mu\text{H}/\text{m}$ . Then, the inductance gradient decreases slowly with speed during the firing process. In the late stage of launch, because the speed of the armature is around  $2 \text{ km}/\text{s}$ , the skin depth is less than  $0.3 \text{ mm}$ , according to Equation (13), which can be noticed as the current tends to cover the surface of the rail completely, so the calculation result is about  $0.7556 \mu\text{H}/\text{m}$ . In the initial stage, since the skin depth can be approximated as constant, the inductance gradient is also kept constant. The electromagnetic thrust of the armature changes with the same general trend of current change; its peak value is approximately  $31 \text{ kN}$ .

In Figure 15, the armature has been in the acceleration state; after  $1.3 \text{ ms}$ , the armature speed curve becomes slower, and the discharge speed is about  $2.216 \text{ km}/\text{s}$ . After  $1.3 \text{ ms}$ , the armature does exhibit approximately uniform linear motion; the movement time of the armature in the rail is about  $1.542 \text{ ms}$ .

The block diagram of the whole system is shown in Figure 16. The test signals of the whole system are divided into three categories: voltage and current of the pulse power supply; magnetic field, voltage, and thermal energy of the launcher; and external ballistic launch velocity.

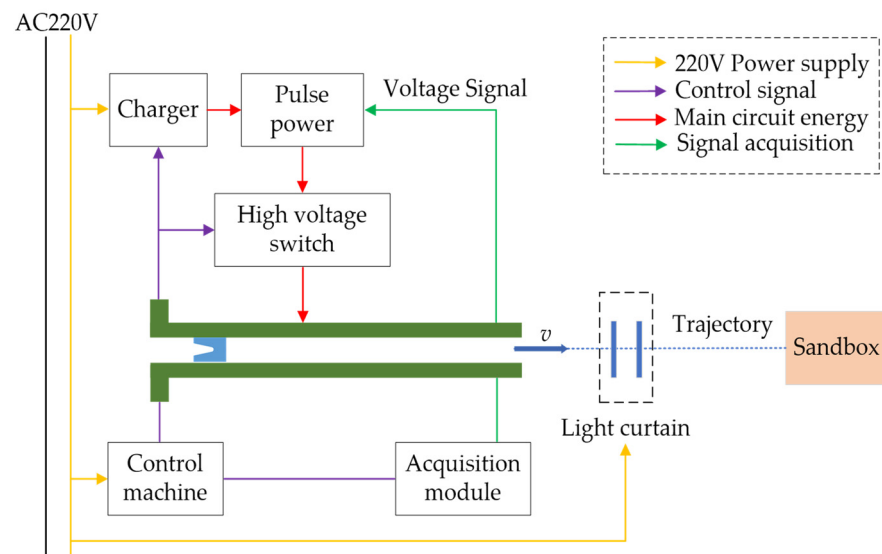


**Figure 16.** The block diagram of the system components.

In the experimental device, the three speed acquisition signals are located in two station light curtain targets. Passing through the signal processing unit, the speed acquisition signals are output to the oscilloscope corresponding channel. The signal acquisition rate is 1 MHz. The armature discharge velocity measured by the light curtain target is approximately 2.296 km/s.

Figure 17 shows the experimental device of the electromagnetic launcher; the length of the rail is 2.18 m, and the mass of the armature in this experiment is about 7 g.



**Figure 17.** The experimental device of the electromagnetic launcher.

The power supply mainly includes voltage and current sensors, which are distributed inside seven power supplies. Sensors such as the B-point coil and bore pressure test signal are located in the transmitter. There are a total of seven voltage sensors that monitor the actual charging voltage of the power module during the charging process. This signal is transmitted to the seven voltage acquisition channels of the measurement system, with a sampling rate of 100 kHz. There are a total of seven current sensors built into seven power sources to monitor the pulse current at the time of power discharge. It adopts the Rogowski coil testing principle to output the differential current signal through an active integrator and transmit it to the seven current acquisition channels of the measurement system, with a sampling rate of 100 kHz. The bore pressure collector, located at the end of the transmitter, collects the transient voltage at both ends of the transmitter rail during electromagnetic emission, corresponding to a test channel signal collection rate of 1 MHz. B-point coil acquisition, also known as B-probe. Located on the side of the transmitter guide rail, it is used to measure the rate of change of the magnetic field in the chamber of the

transmitter during the launch process. This signal corresponds to a test channel acquisition rate of 1 MHz.

Figure 18 shows the burning of the cross-section of the rail before and after the launch, with a layer of wear-resistant steel material on the inner side of the inner rail. In Figure 18, the burning of the cross-section of the rail shows that the current of the inner rail is mainly concentrated on the inner side, while the current of the outer rail is mainly concentrated on the outer side. These results are consistent with the theoretical analysis.

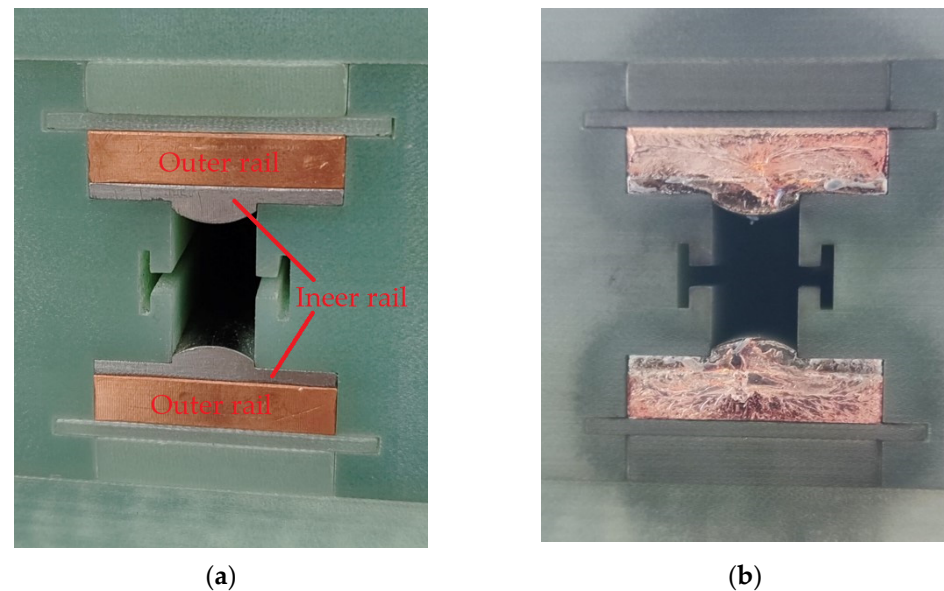


**Figure 18.** The burning of the cross-section of the rail: (a) The cross-section of the rail before the launch; (b) the cross-section of the rail after the launch.

A comparison of the armature discharge speed and armature movement time obtained from the methods in this paper with experimental data is shown in Table 2.

**Table 2.** Comparison table of theoretical analysis and experimental results.

	Discharge Speed		Discharge Moment	
	Value (km/s)	Error (%)	Value (ms)	Error (%)
Experimental results	2.296		1.531	
Calculation results in this paper	2.216	3.484	1.542	0.718

As can be seen from Table 2, the theoretical analysis data and the experimental results are in good agreement, with an error of 3.484% in the discharge speed and 0.718% in the discharge movement. The theoretical analysis data obtained by the method presented in this paper demonstrate good consistency with the experimental results. Compared with experimental data, these errors are all within 5%, which is sufficient to prove the correctness of the method proposed in this paper. Therefore, the application of the research method in this article can achieve an accurate prediction of the discharge velocity of the armature.

## 6. Conclusions

The phenomenon of the skin effect is prevalent in electromagnetic emission, and the skin depth is closely related to the speed of the armature. In this paper, the theoretical formula for the inductance gradient of the augmented electromagnetic rail launcher is derived from the Biot–Savat law, taking into account the effects of the armature speed and the geometry of the launcher on the dynamic inductance gradient. Through rail conversion, the variation law of the dynamic inductance layer of the inner rail and the

mutual inductance layer of the outer rail with the skin depth is obtained. Because of the full consideration of the size of the launcher and the speed of the armature, the inductance gradient theoretical formula proposed in this paper is in line with the actual situation. It is of more reference value in the structural design of the electromagnetic rail launcher.

- (1) From the perspective of the magnetic diffusion equation, the dynamic rail skin depth under the U-shaped armature is obtained, which shows the variation of rail skin depth with the armature speed.
- (2) At the beginning of electromagnetic emission, the armature velocity is small, and the skin depth can be approximated as being related to the current frequency. After the armature velocity exceeds the armature velocity, the skin depth is mainly influenced by the armature velocity and decreases with increasing velocity.
- (3) The inductance gradient is related to the skin depth; the deeper the skin depth of the rail, the larger the value of the inductance gradient. Therefore, the inductance gradient decreases as the armature speed increases.
- (4) The calculation method in this paper is better than the analytical method used in other studies. Therefore, the theoretical formula of the inductance gradient proposed in this paper is in line with the actual situation and has more reference value in the design of an electromagnetic rail launcher.
- (5) The analytical method of the inductance gradient of the electromagnetic rail launcher proposed in this paper, which takes into account the size of the launcher and the speed of the armature, is in better agreement with the experimental results.

**Author Contributions:** Conceptualization, R.Y. and K.A.; methodology, R.Y. and K.A.; software, K.A. and J.J.; validation, K.A. and J.J.; formal analysis, R.Y. and K.A.; investigation, R.Y.; resources, J.J.; data curation, R.Y. and K.A.; writing—original draft preparation, R.Y. and K.A.; writing—review and editing, R.Y. and K.A.; visualization, K.A.; supervision, R.Y. and J.J.; project administration, Q.Y. and R.Y.; funding acquisition, Q.Y. and R.Y. All authors have read and agreed to the published version of the manuscript.

**Funding:** This research was funded by the Major Research Program of the National Natural Science Foundation of China, grant number 92066206, S&T Program of Hebei, grant number 215676146H, and S&T Program of Hebei, grant number 225676163GH.

**Institutional Review Board Statement:** Not applicable.

**Informed Consent Statement:** Not applicable.

**Data Availability Statement:** All data, models generated or used during the study appear in the submitted article.

**Conflicts of Interest:** The authors declare no conflict of interest.

## References

1. Zhu, C.; Li, B. Analysis of sliding electric contact characteristics in augmented railgun based on the combination of contact resistance and sliding friction coefficient. *Def. Technol.* **2020**, *16*, 747–752. [\[CrossRef\]](#)
2. Vertelis, V.; Vincent, G.; Schneider, M.; Balevičius, S.; Stankevič, V.; Žurauskienė, N. Magnetic Field Expulsion From a Conducting Projectile in a Pulsed Serial Augmented Railgun. *IEEE Trans. Plasma Sci.* **2020**, *48*, 727–732. [\[CrossRef\]](#)
3. Li, T.; Feng, G.; Lian, Z.; Liu, S. Simulation Analysis of Inductance Gradient of Series Enhanced Four-Rail Electromagnetic Launcher. *J. Phys. Conf. Ser.* **2020**, *1678*, 012–052. [\[CrossRef\]](#)
4. Cao, R.; Ma, X.; Zhang, G.; Hu, X.; Zhou, Y. Analysis about Change of the Armature's Average Speed for an Experimental Rail Launcher. *IEEE Trans. Electr. Electron. Eng.* **2021**, *16*, 1046–1054. [\[CrossRef\]](#)
5. Praneeth, S.N.; Singh, B.; Khatait, J.P. Study on Effect of Rail Fillet Radius in Electromagnetic Railgun. *IEEE Trans. Plasma Sci.* **2021**, *49*, 2997–3002. [\[CrossRef\]](#)
6. Wen, Y.; Dai, L.; Lin, F. Effect of Geometric Parameters on Equivalent Load and Efficiency in Rectangular Bore Railgun. *IEEE Trans Plasma Sci.* **2021**, *49*, 1428–1433. [\[CrossRef\]](#)
7. Wang, Z.; Yuan, W.; Yan, P. Inductance Gradient for Rail-type Electromagnetic Launcher Under Transient Conditions. *High Volt. Eng.* **2017**, *43*, 4039–4044.
8. Peng, Z.; Wang, G.; Zhai, X.; Zhang, X. Modeling and Analysis of Time-Varying Inductance Gradient for Electromagnetic Rail Launcher. *China Electrotech. Soc.* **2020**, *35*, 4843–4851.

9. Zhai, X.; Li, H.; Liu, H.; Peng, Z. Analysis of dynamic inductance gradient of electromagnetic rail launcher. *J. Natl. Univ. Def. Technol.* **2022**, *40*, 156–163.
10. Ren, S.; Feng, G.; Zhang, P.; Li, T.; Zhao, X. Method of Calculating Inductance Gradient for Complex Electromagnetic Rail Launcher. *Electronics* **2022**, *11*, 2912. [[CrossRef](#)]
11. Tang, L.; Li, H. Simulation Analysis of Railgun in-bore High Magnetic Field. *Comput. Simul.* **2014**, *31*, 1–46.
12. Ruan, J.; Chen, L.; Xia, S.; Wang, Z.; Li, L. A Review of Current Distribution in Electromagnetic Railguns. *China Electrotech. Soc.* **2020**, *35*, 4423–4431.
13. Lv, Q.; Xiang, H.; Lei, B.; Zhang, Q.; Zhao, K.; Li, Z.; Xing, Y. Physical Principle and Relevant Restraining Methods About Velocity Skin Effect. *IEEE Trans. Plasma Sci.* **2015**, *43*, 1523–1530.
14. Wang, Z.; Chen, L.; You, P.; Lan, X.; Ge, Y. Current Distribution Characteristics of Armature-Rail Interface under Velocity Skin Effect and Contact Resistance. *China Electrotech. Soc.* **2022**, *37*, 5003–5010.
15. Li, X.; Lu, J.; Li, Y.; Wu, X. 3-D numerical analysis of distribution characteristics of electromagnetic launcher projectile in-bore magnetic field. *Electr. Mach. Control* **2018**, *22*, 34–40.

**Disclaimer/Publisher’s Note:** The statements, opinions and data contained in all publications are solely those of the individual author(s) and contributor(s) and not of MDPI and/or the editor(s). MDPI and/or the editor(s) disclaim responsibility for any injury to people or property resulting from any ideas, methods, instructions or products referred to in the content.